



King Saud University  
Arabian Journal of Chemistry

www.ksu.edu.sa  
www.sciencedirect.com



ORIGINAL ARTICLE

# The effect of Pt nanoparticles distribution on the removal of cyanide by TiO<sub>2</sub> coated Al-MCM-41 in blue light exposure



Mohammad W. Kadi<sup>a</sup>, A. Hameed<sup>b,c</sup>, R.M. Mohamed<sup>a</sup>, Iqbal M.I. Ismail<sup>a,b,\*</sup>,  
Yaser Alangari<sup>a</sup>, Hui-Ming Cheng<sup>a,d</sup>

<sup>a</sup> Department of Chemistry, Faculty of Science, King Abdulaziz University, P.O. Box 80203, Jeddah 21589, Saudi Arabia

<sup>b</sup> Centre of Excellence in Environmental Studies (CEES), King Abdulaziz University, Jeddah 21589, Saudi Arabia

<sup>c</sup> National Centre for Physics, Quaid-e-Azam University, Islamabad 44000, Pakistan

<sup>d</sup> Shenyang National Laboratory for Materials Science, Institute of Metal Research, Chinese Academy of Sciences, 72 Wenhua Road, Shenyang 110016, China

Received 30 November 2015; accepted 6 February 2016

Available online 15 February 2016

## KEYWORDS

Al-MCM-41;  
Rice Husk;  
Pt loading;  
TiO<sub>2</sub> loaded Al-MCM-41;  
Cyanide

**Abstract** With an aim to enhance the photocatalytic activity, Pt loaded TiO<sub>2</sub>–Al-MCM-41 catalysts with high surface area were synthesized by a multistep route. The waste of the rice processing, rice husk (RH), was used as the precursor for the extraction of silica. The diffuse reflectance and photoluminescence spectroscopy revealed the extension of the absorption edge in the visible region and exciton trapping nature of the dispersed platinum. The structural analysis was carried out by XRD, whereas X-ray photoelectron spectroscopy identified the chemical states of the components of the synthesized powders. The BET surface area measurements revealed the reduction in the surface area and pore volume with the increasing platinum loading. TEM micrographs showed the uniform distribution of TiO<sub>2</sub> and Pt nanoparticles at the surface of Al-MCM-41. The photocatalytic efficiency of the synthesized powders as photocatalysts was obtained for the removal of 100 ppm CN<sup>−</sup> from aqueous solution in fluorescent blue light exposure. Compared to unsupported TiO<sub>2</sub>, the Pt-loaded catalysts exhibited substantially high activity for the removal of CN<sup>−</sup>. A plausible mechanism for the removal of cyanide ions was proposed. The catalysts showed excellent stability and reproducibility in the successive use.

© 2016 The Authors. Production and hosting by Elsevier B.V. on behalf of King Saud University. This is an open access article under the CC BY-NC-ND license (<http://creativecommons.org/licenses/by-nc-nd/4.0/>).

\* Corresponding author at: Department of Chemistry, Faculty of Science, King Abdulaziz University, P.O. Box 80203, Jeddah 21589, Saudi Arabia.

E-mail address: [Iqbal30@hotmail.com](mailto:Iqbal30@hotmail.com) (I.M.I. Ismail).

Peer review under responsibility of King Saud University.



Production and hosting by Elsevier

## 1. Introduction

Photocatalysis is viewed as the potential remediation technology for reducing the concentration of hazardous and carcinogenic pollutants in domestic and industrial wastewater streams (Qamar et al., 2015; Aslam et al., 2016a). Although no doubt  $\text{TiO}_2$  has long been considered as an attractive choice because of its physicochemical properties, availability and low cost, its transparency in the visible region restricts its widespread applications (Cao et al., 2013; Farrokhi et al., 2013). Successive efforts with the variable results were reported in the literature for extending its spectral response and enhancing its photocatalytic activity in the visible region. The incorporation and loading of the noble metals, transition metals, and metals, in an attempt to shorten the band gap and make the material an efficient photocatalyst when exposed to visible light, is an area of interest in this regard (Deng et al., 2012; Mohamed and Baieissa, 2013). Another dimension is the dispersion of nanoparticles of active photocatalysts on supports with a high specific surface area for better interaction of substrate and harvesting of incident photons. The use of advantageous physicochemical properties of the support in the reaction mixture is regarded as an additional advantage (Fan et al., 2008; Huang et al., 2008; Xie et al., 2007, 2008; Yuan et al., 2005, 2008).

Ordered mesoporous materials provide a support medium for metal oxide catalysts and dopants for enhancement of their efficiency. Since its discovery in 1992, MCM-41 has been used as a catalyst in many reactions with the incorporation of metals into its structure. MCM-41 has attracted particular attention and widely used as catalyst hosts for nanomaterials synthesis because of their high specific surface area, uniform pore size and ordered mesoporous channels. It has been documented that the insertion of Al in MCM-41 results in the introduction of ample acidic sites (Ciesla and Schuth, 1999; Junges et al., 1995).

Mesoporous aluminosilicate, Al-MCM-41, is well known to show remarkable acidic properties. Since its pore sizes are larger than those of zeolites, bulky organic substrates can contact acidic sites of mesoporous aluminosilicates. Therefore, Al-MCM-41 molecular sieves have been used to catalyze several organic transformations under vapor or liquid phase reaction conditions (Ito et al., 2011; Iwanami et al., 2012; Ma et al., 2012; Selvaraj et al., 2005; Taguchi and Schüth, 2005). The high specific surface area of Al-MCM-41 makes it a suitable support for photocatalytic processes. Another important research effort is the exploration of low-cost materials, in particular, waste materials for the production of a product of value.

Although cyanide leaching remains the overwhelming option for treating gold ores because of its economy and simplicity of the process, it suffers from toxic and its use poses long-term environmental and disposal problems (Dadgar, 1989; Hiskey and Atluri, 1988). Cyanides are used in a number of chemical synthesis and metallurgical processes (as simple salts or cyanide complexes). Cyanides are highly toxic and must be destroyed or removed from wastewaters prior to discharge. The most common method for treating free or simple cyanide is the alkaline chlorination process. However, chlorination of cyanide results in highly toxic intermediates of cyanogen chloride. These compounds together with the residual chloride create additional environmental problems. Consequently, there is a growing need for alternative, non-chlorine methods for destroying cyanides.

The current study was designed to develop an efficient high surface area visible light active photocatalyst for the removal of highly toxic cyanide ions from water. Al-MCM-41 due to its characteristic surface area and the availability of the surface charges is regarded as an effective support for the better dispersion, spectral response and enhanced absorption of photocatalysts. Adopting an innovative approach, Al-MCM-41 was derived from the silica extracted from the invaluable rice husk. Titania ( $\text{TiO}_2$ ), was loaded on the Al-MCM-41 as the base photocatalyst followed by incorporation of Pt to produce an efficient photocatalyst with a wide-enough band gap that allows the direct absorption of visible photons. The efficiency of the prepared catalyst was tested to remove  $\text{CN}^-$  ion from model wastewater.

## 2. Experimental section

The details of the raw materials, chemicals and procedures adopted for the extraction of silica from waste RH, synthesis of Al-MCM-41 (aluminum-silicates), incorporation of  $\text{TiO}_2$  nanoparticles (NPs) into the synthesized Al-MCM-41, loading of synthesized  $\text{TiO}_2$ -Al-MCM-41 with Pt NPs and evaluation of the photocatalytic activity of the synthesized catalysts for the removal of cyanide ( $\text{CN}^-$ ) ions from the aqueous medium are summarized below.

### 2.1. Silica extraction

The RH obtained from the rice field was thoroughly washed with tap water initially and finally rinsed with deionized water for the removal of accumulated dust and soil. The other chemicals used for the extraction of silica from RH were HCl (37%, Merck), sodium aluminate (54%  $\text{Al}_2\text{O}_3$  + 41%  $\text{Na}_2\text{O}$ , technical grade), NaOH (99%, Carlo-Erba) and KOH (85%, Sigma-Aldrich).

The washed and dried RH was refluxed with HCl to reduce the metallic impurities to the minimal level (Chang et al., 2009). The extraction of silica as sodium silicate with other organic moieties was carried out by stirring the acid treated RH (after drying) with sodium hydroxide solution (Adam and Fua, 2008). The resultant sodium silicate was converted to silica by adding appropriate amounts of mineral acid. The mixture of converted sodium silicate and allied organics from the rice husk was pyrolyzed at 800 °C at a heating and cooling rate of 5 °C/min for 6 h in a muffle furnace (Carbolite) to remove the organic contents. The ashing parameters were similar to those already described in the literature (Chandrasekhar et al., 2006). The processed RH to RHA was subjected to X-ray fluorescence (XRF) analysis for the estimation of the elemental composition of the probable ingredients using an XRF spectrophotometer (Ultima-IV, Rigaku Corporation, Tokyo, Japan). The composition of the as-obtained RHA is presented in Table 1.

### 2.2. Synthesis of Al-MCM-41

The silica extracted from the RH was used to synthesize Al-MCM-41. In a representative synthesis, 53 g silica (synthesized in the previous step) was dissolved in 100  $\text{cm}^3$  of NaOH solution (prepared by dissolving 4.4 g of NaOH in 100 ml distilled water) and stirred with 6 g cetyl trimethyl ammonium bromide (CTAB) for one hour and referred to as “Mixture A”. The “Mixture B” was prepared by stirring 1.0 g  $\text{Al}_2(\text{SO}_4)_3$  (98%, Merck) in 20  $\text{cm}^3$  of 0.5  $\text{cm}^3$  concentrated  $\text{H}_2\text{SO}_4$  solution till

**Table 1** The chemical composition of RHA determined by XRF.

Chemical compositions of RHA	wt%
$\text{SiO}_2$	89.00
$\text{Al}_2\text{O}_3$	1.20
$\text{Fe}_2\text{O}_3$	1.28
$\text{K}_2\text{O}$	1.22
CaO	1.00
C	18.24

clear solution. The mixture B was added to the mixture A under constant stirring to obtain a gel. The gel was transferred to autoclave for hydrothermal treatment under autogenous pressure at 110 °C, for a period of 72 h. The products were filtered, washed with deionized water and dried at 110 °C for 24 h. The as-synthesized samples were calcined at 540 °C for 10 h. The heating and cooling rates were maintained at 5 °C/min.

### 2.3. Synthesis of $\text{TiO}_2$ -Al-MCM-41

The  $\text{TiO}_2$ -Al-MCM-41 was synthesized by conventional ion exchange technique. In a typical synthesis, 1.0 g of Al-MCM-41 was soaked in 100 cm<sup>3</sup> solution of 0.03 M potassium titanium-oxalate and stirred for 24 h. The  $\text{Ti}^{4+}$ -exchanged Al-MCM-41 zeolite sample was filtered, washed with double distilled water to remove the physically adsorbed  $\text{Ti}^{3+}$  species and dried for 24 h in hot air oven at 100 °C. The repeated washing is essential to avoid possible aggregation of  $\text{Ti}^{4+}$  species on the external surface during the calcination process. The resulted  $\text{Ti}^{4+}$ -exchanged zeolite ( $\text{TiO}_2$ -Al-MCM-41) was calcined at 500 °C for 5 h with a heating rate of 5 °C/min. The synthesized  $\text{TiO}_2$  loaded Al-MCM-41 was labeled as “Ti-Al-MCM-41” in the figures and the coming sections.

### 2.4. Synthesis of Pt/TiO<sub>2</sub>-Al-MCM-41 catalyst

Incipient wetness impregnation was used to introduce different wt% of Pt on the surface of Ti-Al-MCM-41. For impregnating Pt on Ti-Al-MCM-41, the appropriate amount of Ti-Al-MCM-41 was soaked in 100 cm<sup>3</sup> of a chloroplatinic acid hexahydrate solution and stirred for 24 h at room temperature. The excessive H<sub>2</sub>O was removed by a rotary evaporator. The Ti-Al-MCM-41 loaded with 0.05%, 0.10%, 0.15% and 0.20% Pt were synthesized and labeled as 0.05% Pt/Ti-Al-MCM-41, 0.10% Pt/Ti-Al-MCM-41, 0.15% Pt/Ti-Al-MCM-41 and 0.20% Pt/Ti-Al-MCM-41.

### 2.5. Characterization of synthesized catalysts

The solid-state absorption spectra of the synthesized powders in the wavelength range of 200–800 nm were recorded by a Perkin Elmer UV–visible diffuse reflectance spectrophotometer (Lambda 650). The band edge positions of the catalysts were estimated by plotting  $(F(R) \times h\nu)^{1/2}$  versus photon energy ( $h\nu$ ), where  $F(R)$  is the Kubelka–Munk transformation of %R data. The photoluminescence (PL) emission spectra of the synthesized powders were recorded by a fluorescence spectrofluorophotometer, RF-5301 PC, Shimadzu, Japan, at an excitation wavelength of 325 nm while the fluorescence emissions were recorded in the range of 350–470 nm. These synthesized powders were characterized by X-ray diffraction, using an Ultima-IV, Rigaku Corporation, Tokyo, Japan, diffractometer with Cu K $\alpha$  radiation ( $\lambda = 1.5418$  Å wavelength at 40 kV accelerating voltage and 30 mA current).

### 2.6. Photocatalytic studies

The procedure adopted for the estimation of the photocatalytic activity of the synthesized catalysts in the removal of cyanide ions ( $\text{CN}^-$ ) under blue light irradiation was similar

to that reported earlier (Baeissa, 2014). In a typical experiment, a Pyrex glass cylindrical batch reactor equipped with a 150 W blue fluorescent lamp and a UV cutoff filter was used for the photocatalytic studies. In a typical experiment, 300 cm<sup>3</sup> of the photocatalyst–cyanide suspension containing the optimized amount of the catalysts was exposed to fluorescent blue light. The optimization of the amount of the catalyst was performed prior to actual photocatalytic studies. The suspension was kept in dark to establish the adsorption and desorption equilibrium. To avoid the evolution of HCN gas, prior to exposure, the pH of the cyanide solution was adjusted to 10.5. The experiments were performed in the natural environment without applying any restriction of pressure and temperature. The samples were collected from the reactor every 5 min in the initial 20 min followed by 10 min till 70 min. After removing the powder by using the disposable 0.22  $\mu\text{m}$  syringe filters, the  $\text{CN}^-_{(\text{aq})}$  concentration was estimated by volumetric titration with  $\text{AgNO}_3$ , using KI as titrant. The removal efficiency of  $\text{CN}^-$  was measured by the comparison of the change in concentration of cyanide ion before and after the exposure.

## 3. Results and discussion

The solid state absorption spectra of Al-MCM-41,  $\text{TiO}_2$ , Ti-Al-MCM-41 and Ti-Al-MCM-41 loaded with 0.05%, 0.1%, 0.15% and 0.20% Pt nanoparticles are presented in Fig. 1. Al-MCM-41 was found completely transparent in the scanning wavelength range of 200 nm to 800 nm. Compared to pure  $\text{TiO}_2$ , a redshift in the absorption edge was observed for  $\text{TiO}_2$  loaded Al-MCM-41. Probably the better dispersion of  $\text{TiO}_2$  at the surface of Al-MCM-41 compared to the bulk resulted in the better spectral response. The view of the normalized absorption spectra of all the powders is presented in the inset of Fig. 1, where an extension of the absorption edge in the visible region is observed with the increase of Pt loading. As the Pt nanoparticles absorb the light with its wavelength below 300 nm (Luo and Imae, 2007), the direct absorption of

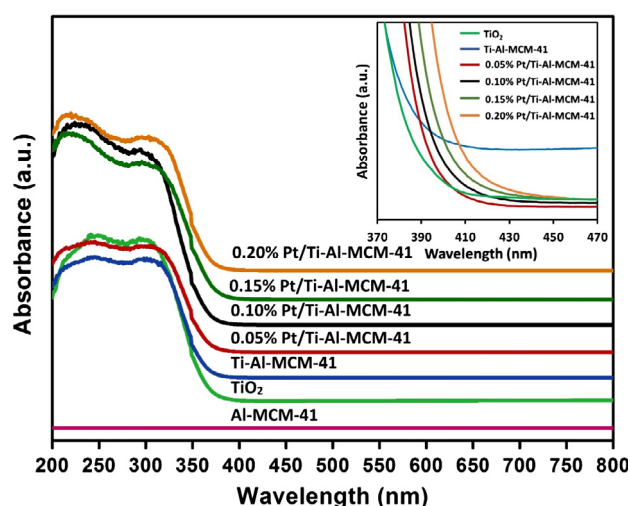


**Figure 1** The comparison of the solid state absorption spectra of Al-MCM-41,  $\text{TiO}_2$ , Ti-Al-MCM-41, 0.05% Pt/Ti-Al-MCM-41, 0.10% Pt/Ti-Al-MCM-41, 0.15% Pt/Ti-Al-MCM-41 and 0.20% Pt/Ti-Al-MCM-41. The inset shows the exploded view in 370–470 nm region.

photons cannot be contributed by surface Pt nanoparticles but by the modified band structures of the surface  $\text{TiO}_2$ . The conduction band of  $\text{TiO}_2$  is dominantly composed of 3d orbitals of  $\text{Ti}^{4+}$  whereas the  $\text{O}^{2-}$  (2p) levels constitute the valence band. Probably, the presence of electron rich Pt ( $5d^9 6s^1$ ) in the vicinity provides the active sites for the low energy transitions from the conduction band of  $\text{TiO}_2$  to Pt at the surface. The magnitude of the absorption increases with the increase in the surface density of Pt nanoparticles. Additionally, the role of d–d transitions between the closely spaced  $\text{Ti}^{4+}$  and  $\text{Pt}^0$  states for enhanced absorption cannot be neglected. The band edges of the synthesized powders were obtained by plotting  $(F(R) \times h\nu)^{1/2}$  versus photon energy ( $h\nu$ ), where  $F(R)$  is the Kubelka–Munk transformation of the % $R$  (reflectance) data. The evaluated band gaps of the synthesized powders are presented in Table 2. The evaluated band gap value of  $\sim 3.1$  eV for  $\text{TiO}_2$  powder was in accordance with the literature values (Navarro et al., 2009). A gradual decrease in the band gap was observed with the increasing Pt loading.

The comparison of the PL spectra of Pure  $\text{TiO}_2$ , Ti–Al–MCM-41 and 0.05%, 0.1%, 0.15% and 0.20% Pt nanoparticles loaded Ti–Al–MCM-41 powders is presented in Fig. 2. For pure  $\text{TiO}_2$ , the intense emission band appears at 402 nm (3.1 eV) that corresponds to the de-excitation from  $\text{Ti}^{4+}$  (3d)  $\rightarrow$  O(2p). The observed value is in accordance with the literature for rutile  $\text{TiO}_2$  (Abazović et al., 2009) and further confirms the evaluation of the band gaps by UV–visible diffuse reflectance spectroscopy. Due to the probable matrix and the dispersion effect, a redshift of 9 nm in the emission band was observed for  $\text{TiO}_2$  loaded Al–MCM-41. For the Pt-loaded powders, a substantial decrease in the intensity of the emission band at 411 nm was noticed. This observation is valuable from photocatalysis as it suggests the electron trapping ability of the species present in the vicinity. The successive decrease in the intensity of the emission band clearly indicates the enhanced charge trapping with the increasing Pt loading. A significant decrease of  $\sim 60\%$  in the intensity for 0.20% Pt/Ti–Al–MCM-41 was observed.

The XRD patterns of Al–MCM-41, Ti–Al–MCM-41 and 0.05%, 0.1%, 0.15% and 0.20% Pt nanoparticles loaded Ti–Al–MCM-41 powders in the  $2\theta$  range of  $2^\circ$ – $8^\circ$  are presented in Fig. 3. The characteristic reflections in the XRD pattern of MCM-41 correspond to (100), (110) and (200) hexagonal planes and are regarded as the characteristic of highly ordered MCM-41 (Savidha et al., 2003). The sharpness of the (100) reflection in the XRD pattern of the Al–MCM-41 reveals that the insertion of Al does not disturb the ordered hexagonal structure (Chang et al., 2011). The reduction in peak intensity of Ti–Al–MCM-41 sample compared with that of Al–MCM-41

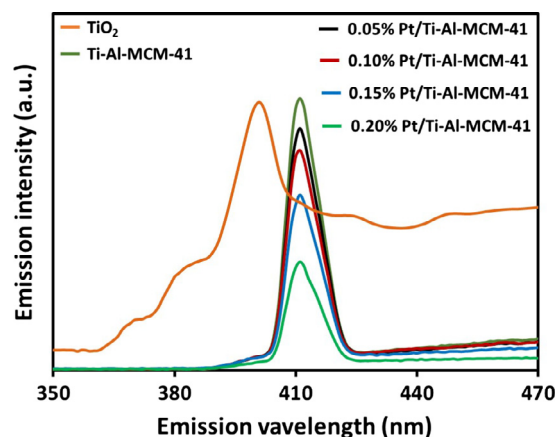


**Figure 2** The PL spectra of  $\text{TiO}_2$ , Ti–Al–MCM-41, 0.05% Pt/Ti–Al–MCM-41, 0.10% Pt/Ti–Al–MCM-41, 0.15% Pt/Ti–Al–MCM-41 and 0.20% Pt/Ti–Al–MCM-41.

indicates the surface coverage of MCM-41 with the deposition of  $\text{TiO}_2$ . Although the successive decrease in the intensity indicated the increased surface coverage by Pt nanoparticles, however, the retention in the peak position negates any significant change in the ordered MCM-41 structure. Due to the highly ordered crystalline nature and low concentration, the reflections due to  $\text{TiO}_2$  were masked by that of Al–MCM-41. The careful analysis of very low-intensity reflections at  $25.23^\circ$ ,  $37.56^\circ$  and  $48.32^\circ$  revealed the formation of anatase phase (JCPDS 21-1272). Among the additional reflections, the reflection at  $2\theta$  values of  $27.4^\circ$  evidenced the formation of rutile  $\text{TiO}_2$  in the minor proportion.

The variations in the BET specific surface area ( $\text{m}^2/\text{g}$ ) and the pore volumes ( $\text{cm}^3/\text{g}$ ) of the synthesized powders in comparison with A–MCM-41 are presented in the Fig. 4. All the synthesized powders exhibit high BET surface area of  $> 800 \text{ m}^2/\text{g}$ , which is the characteristic of mesoporous materials. Compared to Al–MCM-41, a successive decrease in the surface area for both  $\text{TiO}_2$  and Pt deposited  $\text{TiO}_2$  was noticed, suggesting the independence of the nature of the deposited

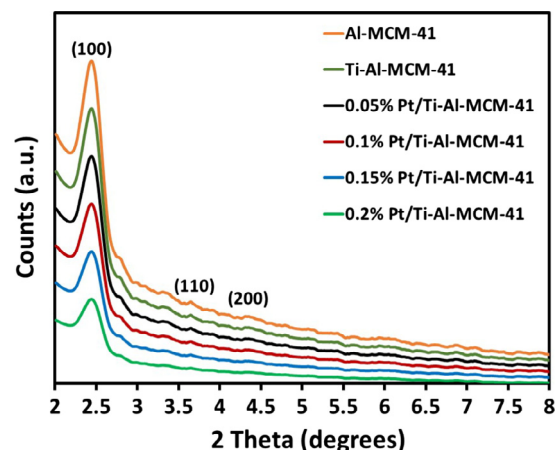


**Figure 3** The XRD patterns of Al–MCM-41, Ti–Al–MCM-41, 0.05% Pt/Ti–Al–MCM-41, 0.10% Pt/Ti–Al–MCM-41, 0.15% Pt/Ti–Al–MCM-41 and 0.20% Pt/Ti–Al–MCM-41 in the  $2\theta$  range of  $2^\circ$ – $8^\circ$ .

**Table 2** The evaluated band gaps of the synthesized materials.

Sample	Band gap energy (eV)
Al–MCM-41	Non-absorptive
Ti–Al–MCM-41	3.15
$\text{TiO}_2$	3.02
0.05% Pt/Ti–Al–MCM-41	2.94
0.10% Pt/Ti–Al–MCM-41	2.89
0.15% Pt/Ti–Al–MCM-41	2.79
0.20% Pt/Ti–Al–MCM-41	2.72



materials. The decrease of pore volumes was also observed with TiO<sub>2</sub> loading on the Al-MCM-41 as well as the increase of Pt loading on Ti-Al-MCM-41 for all the catalysts as a result of the coverage of the pores by the dispersed entities.

The deconvoluted peaks of Al2p, Si2p, Ti2p, O1s and Pt4f, and the components of Pt dispersed Ti-Al-MCM-41, acquired for 0.20% Pt loaded sample are presented in Fig. 5a–e. The deconvolution of Al2p revealed a single peak centered at 74.12 eV and represented the Al in 3+ oxidation state. Similarly, a single Si2p peak positioned at 102.92 eV was designated to Si in 4+ oxidation states in zeolites. Due to the spin-orbit coupling, the Ti2p appears as a doublet composed of Ti2p<sub>3/2</sub> and Ti2p<sub>1/2</sub>. The deconvolution of both the components reveals no additional peak. The Ti2p<sub>1/2</sub> and Ti2p<sub>3/2</sub> appeared at the binding energy values of 464.33 eV and 458.53 eV. The observed values were in close agreement with those reported for Ti<sup>4+</sup> in TiO<sub>2</sub> (NIST-XPS database). The deconvolution of the high-resolution scanning of O1s core levels reveals additional peaks due to the various chemical environments. The intense peak centered at 531.53 eV was assigned to the hydroxyl groups associated with Al<sup>3+</sup> whereas the low-intensity peak at 532.8 eV was identified as the oxygen groups attached to Si<sup>4+</sup>. Another low-intensity peak at 529.0 eV was assigned to the oxygen grouped with Ti<sup>4+</sup>. The deconvolution of the split Pt4f core levels shows no additional peak except for the split Pt4f<sub>7/2</sub> at 71.4 eV and Pt4f<sub>5/2</sub> at 74.62 eV. The peak positions of the Pt4f split levels confirm the presence of Pt in zero valent states.

The comparison of the HRTEM images of Al-MCM-41, Ti-Al-MCM-41 and Pt loaded Ti-Al-MCM-41 powders is presented in Fig. 6. The image of Al-MCM-41 shows the uniformly shaped particles of variable sizes ranged between 10 and 30 nm. The TEM image of Ti-Al-MCM-41 shows that the loaded TiO<sub>2</sub> particles, pointed by the yellow arrows, are prominent at the surface of Al-MCM-41. The TiO<sub>2</sub> particles with an estimated particle size of < 10 nm are well dispersed on the whole surface. As pointed by the red arrows, the images of the Pt-loaded Ti-Al-MCM-41 powder revealed the uniform distribution of Pt nanoparticles. An increase in the particle density can be observed with the increased Pt loading. No sig-

nificant change in the morphology of Al-MCM-41 particles was observed with TiO<sub>2</sub> or Pt loading.

The aqueous phase photocatalysis in the natural environment is based on the generation of the reactive oxygen species (ROS) with the absorption of photons by the semiconductor particles. The superoxide anion radicals (O<sub>2</sub><sup>•−</sup>) and hydroxyl radicals (•OH) are regarded as the primary ROS generated as a consequence of oxygen reduction and water oxidation, respectively. The suitability of the potential of the valence and conduction band edges is the crucial criterion that predicts the populations of these species in the medium. Another important parameter is the pH value of the system that supports the lifetime of these species in the system. The generation of these ROS can be represented by the following equations (Aslam et al., 2014, 2016b; Hameed et al., 2015):



Although the further interaction of these primary ROS with the water molecules generates a cascade of a variety of other species including H<sub>2</sub>O<sup>•+</sup> and H<sub>2</sub>O<sub>2</sub>, their specific role in interacting with the substrates present in the system is not well-defined. Besides oxidizing the adsorbed H<sub>2</sub>O molecules, the oxidation of the adsorbed substrates by the photon to generate holes (h<sup>+</sup>) is also well documented (Hoffmann et al., 1995).

Prior to the practical photocatalytic studies, rough experiments with the minimal amount of 0.5 g/l of the catalysts were carried out to approximate the optimum performance catalyst. Based on the rough estimation, the amount of the catalyst for prime removal of CN<sup>−</sup> ion in the total span of 60 min was optimized by performing the experiments with the variable amounts of the 0.20% Pt loaded catalyst ranging from 0.4 g/l to 1.6 g/l with a step of 0.2 g/l till 1.2 g/l and 0.4 g/l afterward. The comparison of time-dependent CN<sup>−</sup> removal profiles for each catalyst loading is presented in Fig. 7. A gradual incremental linear increase in the removal efficiency was observed with the increasing catalyst loading till 1.2 g/l. Although the removal of CN<sup>−</sup> experiences a mild increase afterward for 1.6 g/l loading, the increment was not as substantial as in the case of 1.2 g/l. The increased activity elaborated the enhanced absorption of photons with the increasing catalyst particle density that is saturated at the catalyst loading of 1.2 g/l. The further increase beyond 1.2 g/l probably results in the decrease of the total number of effective photons due to the shielding by the excessive catalyst particles. To elucidate the above discussion further, the comparison of the variations in the removal of CN<sup>−</sup> ions at the intervals of 10 min, 30 min and 60 min as a function of the catalyst loading is presented in the inset of Fig. 7.

The activity of the synthesized photocatalysts was compared for the removal of cyanide ions in the aqueous phase. The experiments were performed in the natural experiment. Based on the observations of the preceding study, the optimized amount of 1.2 g/l of each catalyst was used in the photocatalytic removal experiments. The dark experiments revealed a comparatively high adsorption of CN<sup>−</sup> substrate on pure and Pt-dispersed Ti-Al-MCM-41 catalysts as compared to pure TiO<sub>2</sub> powder. Compared to ~13% for the bare TiO<sub>2</sub>, ~21% adsorption of CN<sup>−</sup> ions was observed on pure

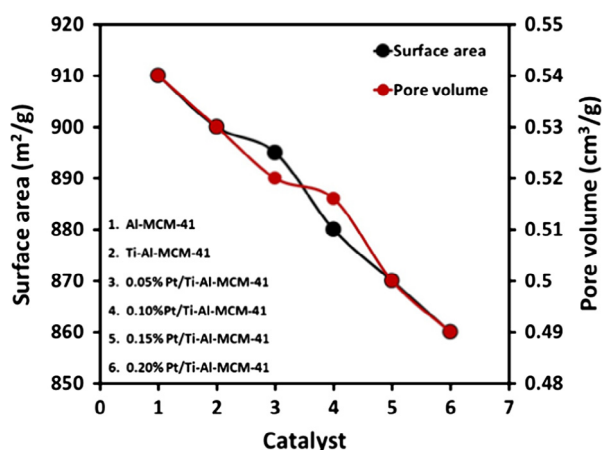


**Figure 4** The variations in the BET surface area (m<sup>2</sup>/g) and the pore volumes (cm<sup>3</sup>/g) of the synthesized powders in comparison with Al-MCM-41.

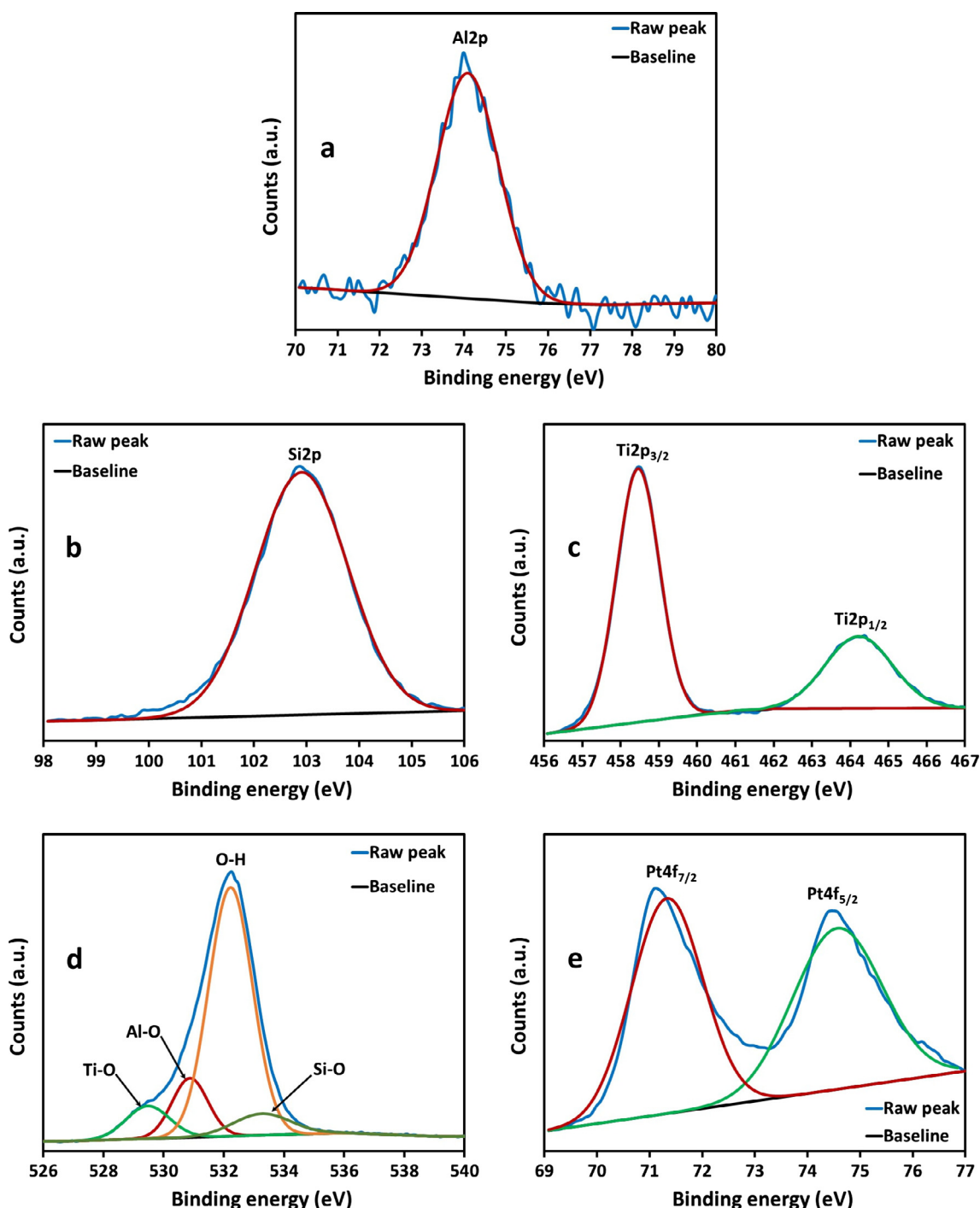


**Figure 5** The de-convoluted narrow angle core level XPS scans of (a) Al2p (b) Si2p (c) Ti2p (d) O1s and (e) Pt4f acquired for 0.20% Pt/Ti-Al-MCM-41 for the estimation of variations in oxidation states.

and Pt-dispersed Ti-Al-MCM-41 powders. The higher surface area of the Al-MCM-41 supported catalysts with significantly higher number of active sites compared to pure TiO<sub>2</sub> powder can be regarded as the plausible cause of this effect. Interestingly, no significant effect of the Pt dispersion was observed. The comparison of the photocatalytic removal of CN<sup>-</sup> ions as a function of time over unsupported TiO<sub>2</sub>, Ti-Al-MCM-41 and Pt dispersed Ti-Al-MCM-41 under blue light (450–500 nm) irradiation, is presented in Fig. 8a. In the initial

10 min of blue light exposure, the unsupported TiO<sub>2</sub> removed ~3%, whereas Ti-Al-MCM-41, 0.05% Ti-Al-MCM-41, 0.10% Ti-Al-MCM-41, 0.15% Ti-Al-MCM-41 and 0.20% Ti-Al-MCM-41 removed ~6%, ~28%, ~43%, ~51% and ~52% of the CN<sup>-</sup> substrate, respectively. In half-hour of exposure, ~6% of the CN<sup>-</sup> was removed by unsupported TiO<sub>2</sub>, whereas double amount was removed by TiO<sub>2</sub> dispersed on Al-MCM-41. The removal of the CN<sup>-</sup> in the same period for 0.05% Ti-Al-MCM-41, 0.10% Ti-Al-MCM-41, 0.15%

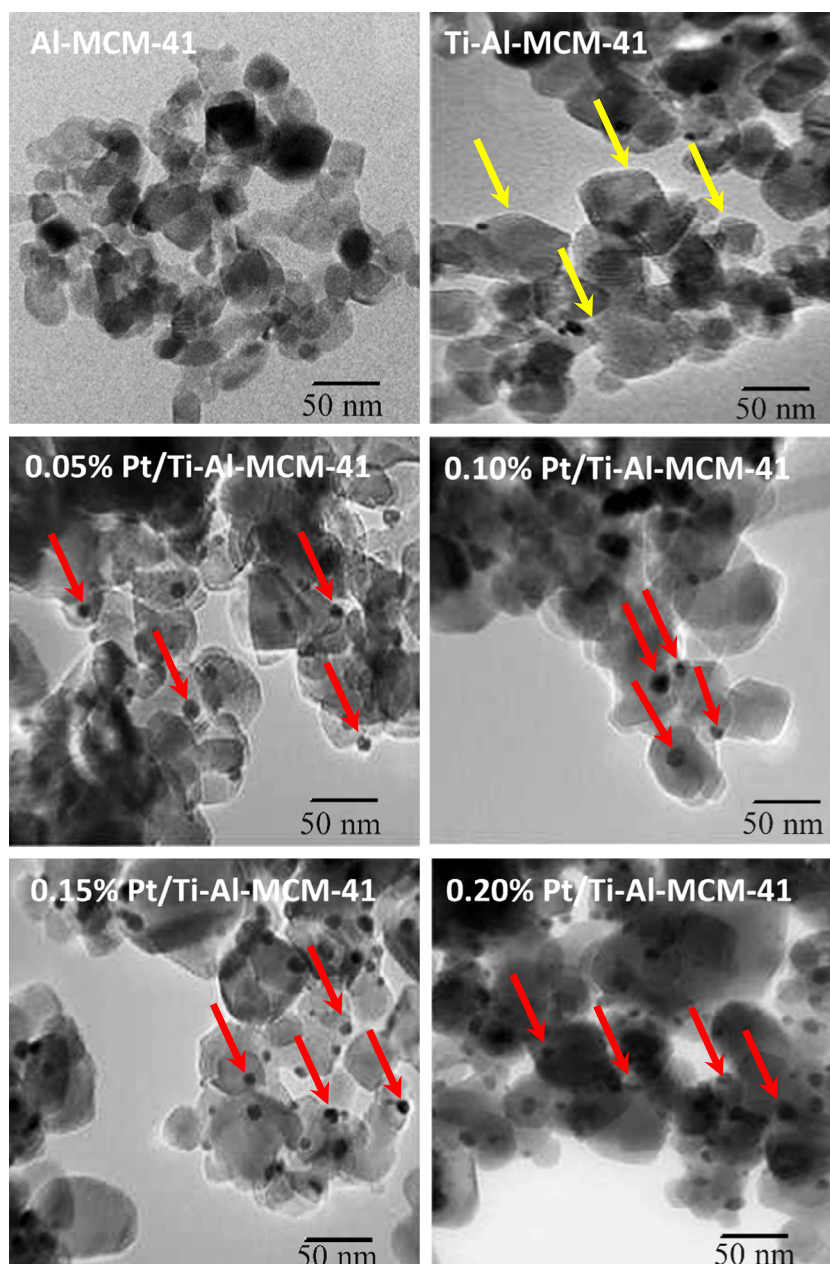


**Figure 6** The HRTEM images of Al-MCM-41, Ti-Al-MCM-41 and Pt loaded Ti-Al-MCM-41 catalysts. The yellow arrows in the image of Ti-Al-MCM-41 identify the  $\text{TiO}_2$  NPs whereas the red arrows highlight the Pt NPs.

Ti-Al-MCM-41 and 0.20% Ti-Al-MCM-41 was 44%, 63%, 75% and 76%, respectively. Compared to the 14% and 21% removal for the unsupported and Al-MCM-41 supported  $\text{TiO}_2$ , the Pt-loaded Ti-Al-MCM-41 removed 66%, 85%, 99.5% and 100% of  $\text{CN}^-$  ions in 70 min of blue light exposure. The effect of the Pt loading on the rate of  $\text{CN}^-$  removal was estimated by applying the Langmuir–Hinshelwood kinetic model for pseudo-first order reactions. The plots of the  $\ln(C_0/C)$  versus the blue light exposure time are presented in Fig. 8b. The validation of the kinetic model with the linear increase in the rate of removal of  $\text{CN}^-$  ions was observed for pure  $\text{TiO}_2$ , Ti-Al-MCM-41, 0.05% Pt/Ti-Al-MCM-41 and 0.10% Pt/Ti-Al-MCM-41 catalysts, whereas a deviation was observed for 0.15% and 0.20% Pt loaded Ti-Al-MCM-41. These annotations led to the conclusion that the Lang-

muir–Hinshelwood kinetic model does not hold well for fast experiments. Interestingly the rate of  $\text{CN}^-$  removal by the  $\text{TiO}_2$  dispersed on Al-MCM-41 was higher than that of the unsupported  $\text{TiO}_2$ . The higher surface area of Ti-Al-MCM-41 as well as the extension of the absorption edge in the visible region (the inset of Fig. 1), regulates a higher number of photons for the photocatalytic process. The higher removal rate indicates the supporting role of the Pt nanoparticles dispersed Ti-Al-MCM-41 in enhancing the photocatalytic activity. The observation suggests that the surface Pt nanoparticles facilitate the enhanced absorption of photons by lowering the conduction band edge and also serve as the trap and transfer centers for the excited electrons. The photoexcited electrons from the conduction band of the  $\text{TiO}_2$  are initially trapped in  $5d^9 + 6s^1$  states of the Pt and finally transferred to the



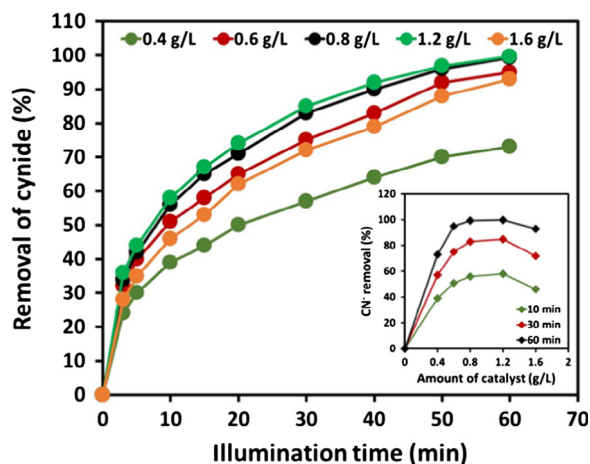


**Figure 7** The effect of the catalyst loading (0.20% Pt/Ti-Al-MCM-41) on the photocatalytic removal (%) whereas the inset shows the variations in percentage cyanide with the changing catalyst loading.

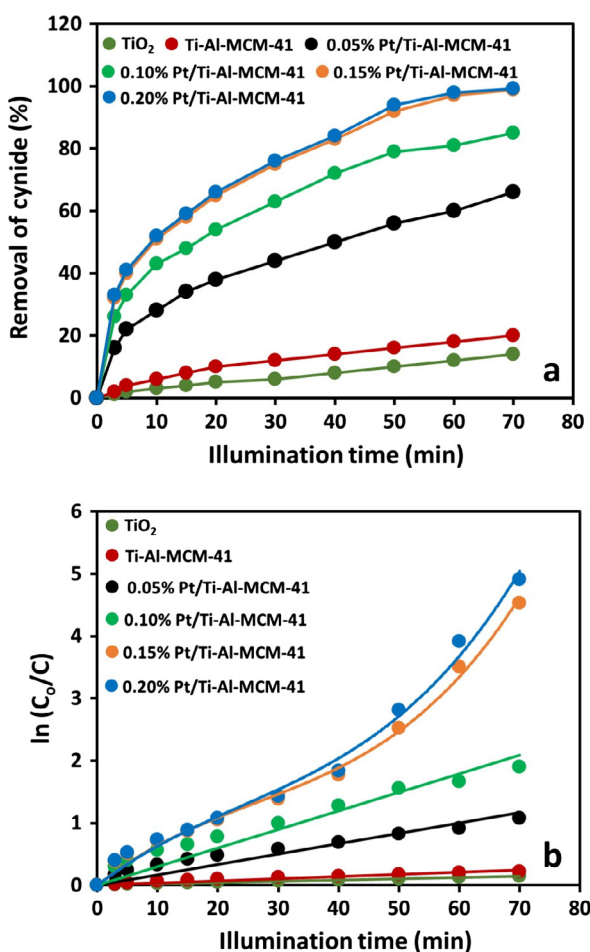
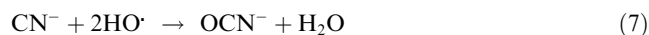
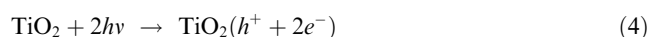


**Figure 8** The effect of the Pt loading on the (a) percentage removal and (b) the rate of removal of cyanide ions.

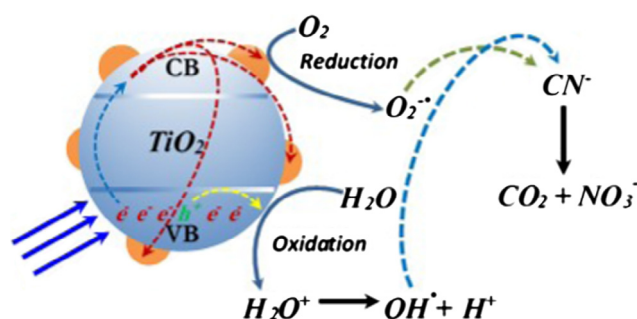
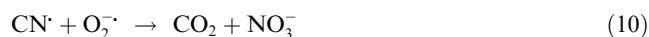
adsorbed  $O_2$ . The reduction of the adsorbed oxygen (Eq. (1)) results in the formation of superoxide anion radicals ( $O_2^{\cdot-}$ ). The desorption of the superoxide anion radicals ( $O_2^{\cdot-}$ ) from

the surface and their mobility in the solution is already established (Kwon and Yoon, 2009). As a consequence of the trapping of the conduction band electrons by the Pt states, the extended lifetime of the photogenerated holes ( $h^+$ ) results in the enhanced production of hydroxyl radicals ( $\cdot OH$ ) by water oxidation (Eqs. (2) and (3)). The escalated rate of  $CN^-$  removal for the higher Pt loadings of 0.15% and 0.20%, especially with the decreasing concentration indicates the availability of higher ROS for each  $CN^-$ . The above-mentioned discussion can be summarized pictorially as given in Scheme 1.

A few studies are available in the literature that describes the photocatalytic removal of  $CN^-$  ions from the aqueous medium. Approximately all the studies were based on the narration of the results or the parametric effect on the photocatalytic removal of cyanide. The removal mechanism is rarely discussed. The illustrated mechanism in the literature (Ibrahim et al., 2013; Phillips, 1983) for the oxidation of  $CN^-$  in the presence of  $O_2$  is narrated by the set of equations below:



Based on the lifespan and generation mechanism of hydroxyl radicals (Pichat, 2013), the above-mentioned mechanism does not properly validate the removal of  $CN^-$  ions. Considering the negatively charged nature of the cyanide ions, the presence of the ROS (superoxide anions and hydroxyl radicals) and the photon generated oxidation site (i.e.  $h^+$  in the photocatalytic system), it might be presumed that oxidation is the only plausible pathway for the removal of  $CN^-$  ions. It is anticipated that the removal of  $CN^-$  in the photocatalytic system is a multistep process initiated by the interaction of  $CN^-$  ions with the photogenerated holes ( $h^+$ ). This leads to the formation of the neutral  $CN^\cdot$  radicals that are further interacted by the superoxide anion and hydroxyl radicals for mineralization. The same may be illustrated by the following equations:



**Scheme 1** The plausible mechanism of  $CN^-$  removal.



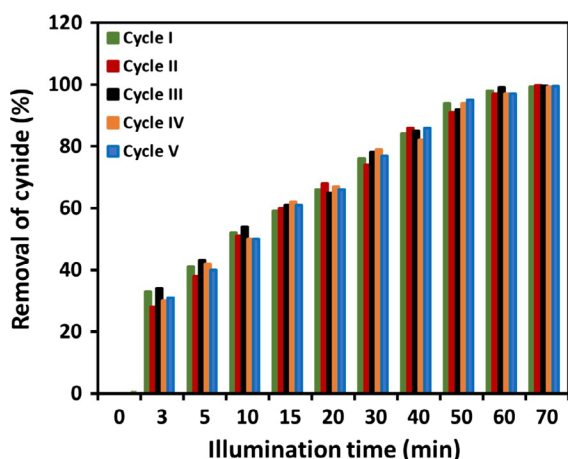


**Figure 9** The photocatalytic performance and reusability of the catalyst (0.20% Pt/Ti-Al-MCM-41) in successive five cycles.

As presented in Fig. 9, the stability and reusability of 0.20% Pt loaded Ti-Al-MCM-41 was investigated for five successive cycles under identical experimental conditions. The catalyst shows a stable response with the acceptable variations in the activity.

#### 4. Conclusion

The study demonstrated that the waste materials such as rice husk can be utilized for the extraction of the raw materials for the valuable products. The Al-MCM-41 derived from the silica, extracted from the rice husk, was compatible with that produced by the costly chemical. The distribution of TiO<sub>2</sub> at the high surface area material such as Al-MCM-41 resulted in the enhanced activity compared to low surface area unsupported powder. The presence of the Pt nanoparticles in the low fraction at the surface of TiO<sub>2</sub> supported on the high surface area Al-MCM-41 not only extends its light spectral response but also facilitates the enhanced production of ROS for its higher photocatalytic CN<sup>-</sup> removal efficiency. Along with the ROS generated in the system, the photogenerated holes also participate in the CN<sup>-</sup> removal process.

#### Acknowledgments

This project was funded by the Deanship of Scientific Research (DSR), King Abdulaziz University, Jeddah, under Grant No. 50-130-35-HiCi. The authors, therefore, acknowledge with thanks DSR for technical and financial support.

#### References

- Abazović, N.D., Mirengi, L., Janković, I.A., Bibić, N., Sojić, D.V., Abramović, B.F., Comor, M.I., 2009. *Nanoscale Res Lett.* 4, 518–525.
- Adam, F., Fua, H.K., 2008. Production of silica from biogenic material. Malaysian Patent MY-136715-A.
- Aslam, M., Ismail, I.M.I., Chandrasekaran, S., Hameed, A., 2014. *J. Hazard. Mater.* 276, 120–128.
- Aslam, M., Qamar, M.T., Soomro, M.T., Ismail, I.M.I., Ahmed, R.Z., Ashraf, M.W., Hameed, A., 2016a. *RSC Adv.* 6, 2436–2449.
- Aslam, M., Qamar, M.T., Soomro, M.T., Ismail, I.M.I., Salah, N., Almeelbi, T., Gondal, M.A., Hameed, A., 2016b. *Appl. Catal. B* 180, 391–402.

- Baeissa, E.S., 2014. *J. Ind. Eng. Chem.* 20, 3761–3766.
- Cao, Y., Yu, Y., Zhang, P., Zhang, L., He, T., Cao, Y., 2013. *Sep. Purif. Technol.* 104, 256–262.
- Chang, Y.C., Bai, H., Li, S.N., Kuo, C.N., 2011. *Sensors* 11, 4060–4072.
- Chang, F.W., Yang, H.C., Roselin, L.S., Kuo, W.Y., 2009. *Appl. Catal. A* 304, 30–39.
- Chandrasekhar, S., Pramada, P.N., Majeed, J., 2006. *J. Mater. Sci.* 41, 7926–7933.
- Ciesla, U., Schuth, F., 1999. *Microporous Mesoporous Mater.* 27, 131–149.
- Dadgar, A., 1989. *J. Met.* 41, 37–41.
- Deng, F., Li, Y., Luo, X., Yang, L., Tu, X., 2012. *Colloids Surf., A* 395, 183–189.
- Fan, X.X., Chen, X.Y., Zhu, S.P., Li, Z.S., Yu, T., Ye, J.H., Zou, Z. G., 2008. *J. Mol. Catal. A: Chem.* 284, 155–160.
- Farrokhi, M., Yang, J., Lee, S., Shirzad-Siboni, M., 2013. *J. Environ. Health Sci. Eng.* 11, 23–28.
- Hameed, A., Aslam, M., Ismail, I.M.I., Salah, N., Fornasiero, P., 2015. *Appl. Catal. B* 163, 444–451.
- Hiskey, J.B., Atluri, V.P., 1988. *Miner. Process. Extract. Metall. Rev.* 4, 95–134.
- Hoffmann, M.R., Martin, S., Choi, W., Bahnemann, D.W., 1995. *Chem. Rev.* 95, 69–96.
- Huang, J.H., Wang, X.C., Hou, Y.D., Chen, X.F., Wu, L., Wang, X. X., Fu, X.Z., 2008. *Microporous Mesoporous Mater.* 110, 543–552.
- Ibrahim, I.A., Ismail, A.A., Mohamed, R.M., 2013. *Eur. J. Miner. Process. Environ. Protect.* 3, 281–290.
- Ito, S., Hayashi, A., Komai, H., Yamaguchi, H., Kubota, Y., Asami, M., 2011. *Tetrahedron* 67, 2081–2089.
- Iwanami, K., Seo, H., Choi, J.C., Sakakura, T., Yasuda, H., 2012. *Tetrahedron* 66, 1898–1901.
- Junges, U., Jacobs, W., Martin, I.V., Krutzsch, B., Schüth, F., 1995. *J. Chem. Soc., Chem. Commun.*, 2283–2284.
- Kwon, B.G., Yoon, J., 2009. *Bull. Korean Chem. Soc.* 30, 667–670.
- Luo, X., Imae, T., 2007. *J. Mater. Chem.* 17, 567–571.
- Ma, F., Chen, S., Wang, Y., Chen, F., Lu, W., 2012. *Appl. Catal. A* 427–428, 145–154.
- Mohamed, R.M., Baeissa, E.S., 2013. *J. Alloys Compd.* 558, 68–72.
- Navarro, R.M., Del Valle, F., Villoria de la Mano, J.A., Álvarez-Galván, M.C., Fierro, J.L.G., 2009. *Adv. Chem. Eng. Photocatal. Technol.* 36, 111–143.
- NIST-XPS database, version 3.5. <<http://srdata.nist.gov/xps/>>.
- Phillips, R., 1983. *Sources and Application of Ultraviolet Radiation*. Academic Press, New York, pp. 124.
- Pichat, P., 2013. *Photocatalysis and Water Purification: From Fundamentals to Recent Applications*, first ed. Wiley-VCH Verlag, Weinheim, Germany.
- Qamar, M.T., Aslam, M., Ismail, I.M.I., Salah, N., Hameed, A., 2015. *ACS Appl. Mater. Interfaces* 7, 8757–8769.
- Savidha, R., Pandurangan, A., Palaichamy, M., Murugesan, V., 2003. *Catal. Lett.* 91, 49–61.
- Selvaraj, M., Jeon, S.H., Han, J., Sinha, P.K., Lee, T.G., 2005. *Appl. Catal. A* 286, 44–51.
- Taguchi, A., Schüth, F., 2005. *Microporous Mesoporous Mater.* 77, 1–45.
- Xie, Y., Li, Y.Z., Zhao, X.J., 2007. *J. Mol. Catal. A: Chem.* 277, 119–126.
- Xie, Y., Zhao, X.J., Li, Y.Z., Zhao, Q.N., Zhou, X.D., Yuan, Q.H., 2008. *J. Solid State Chem.* 181, 1936–1942.
- Yuan, S., Sheng, Q.R., Zhang, J.L., Chen, F., Anpo, M., Zhang, Q.H., 2005. *Microporous Mesoporous Mater.* 79, 93–99.
- Yuan, S., Sheng, Q.R., Zhang, J.L., Yamashita, H., He, D.N., 2008. *Microporous Mesoporous Mater.* 110, 501–507.